ELSEVIER

International Journal of Solids and Structures 40 (2003) 7539–7552

INTERNATIONAL JOURNAL OF SOLIDS and STRUCTURES

www.elsevier.com/locate/ijsolstr

Modeling quasi-static crack growth with the extended finite element method Part II: Numerical applications

R. Huang [a], N. Sukumar [b,*], J.-H. Prévost [c]

[a] *Department of Aerospace Engineering & Engineering Mechanics, The University of Texas at Austin, Austin, TX 78712, USA*
[b] *Department of Civil and Environmental Engineering, University of California, One Shields Avenue, Davis, CA 95616, USA*
[c] *Department of Civil and Environmental Engineering, Princeton University, Princeton, NJ 08544, USA*

Received 30 October 2002; received in revised form 3 June 2003; accepted 7 August 2003

Abstract

In Part I [Int. J. Solids Struct., 2003], we described the implementation of the extended finite element method (X-FEM) within Dynaflow™, a standard finite element package. In our implementation, we focused on two-dimensional crack modeling in linear elasticity. For crack modeling in the X-FEM, a discontinuous function and the near-tip asymptotic functions are added to the finite element approximation using the framework of partition of unity. This permits the crack to be represented without explicitly meshing the crack surfaces and crack propagation simulations can be carried out without the need for any remeshing. In this paper, we present numerical solutions for the stress intensity factor for crack problems, and also conduct crack growth simulations with the X-FEM. Numerical examples are presented with a two-fold objective: first to show the efficacy of the X-FEM implementation in Dynaflow™; and second to demonstrate the accuracy and versatility of the method to solve challenging problems in computational failure mechanics.

Keywords: Strong discontinuities; Partition of unity; Extended finite element; Crack propagation; Bimaterial interface; Mud-crack; Channel-cracking; Thin films

1. Introduction

In a prior study (Sukumar and Prévost, 2003) (referred to hereafter as Part I), we have described the implementation of the extended finite element method (X-FEM) for the modeling of crack discontinuities within Dynaflow™ (Prévost, 1983), a standard finite element package. The methodology adopted for modeling crack discontinuities falls within the purview of the X-FEM (Moës et al., 1999; Daux et al., 2000),

* Corresponding author. Tel.: +1-530-7546415; fax: +1-530-7527872.
E-mail address: nsukumar@ucdavis.edu (N. Sukumar).

0020-7683/$ - see front matter © 2003 Elsevier Ltd. All rights reserved.
doi:10.1016/j.ijsolstr.2003.08.001

which is a particular instance of the partition of unity method (Melenk and Babuška, 1996; Duarte and Oden, 1996).

In the X-FEM, special functions are added to the finite element approximation using the framework of partition of unity. For crack modeling, a discontinuous function and the two-dimensional asymptotic crack-tip displacement fields are used to account for the crack. This enables the domain to be modeled by finite elements without explicitly meshing the crack surfaces. Hence, crack propagation can be simulated without any user-intervention or the need to remesh as the crack advances. For additional details and an exhaustive list of references on the X-FEM and related methods, the interested reader can refer to Part I.

In this paper, we focus our attention on the application of the X-FEM to crack problems in isotropic and bimaterial media. Numerical examples are presented to demonstrate the accuracy of the numerical technique and to show its versatility to solve challenging problems in computational failure mechanics.

2. Numerical applications

We present numerical results for the computation of the stress intensity factors (SIFs) and also study crack propagation simulations in isotropic and layered materials. First, three benchmarks problems in linear isotropic elasticity are considered with the following objectives:

- To verify and test the X-FEM implementation in Dynaflow™;
- To show the accuracy obtainable on unstructured as well as structured meshes that are relatively coarse at the crack-tip; and
- To study domain independence in the SIF computations.

Then, in keeping with the strength of the X-FEM, we present crack propagation simulations that reveal the potential of the technique. In particular, first a brittle crack growth simulation in a double cantilever beam is carried out, and then a mud-crack pattern is simulated to illustrate the advanced crack growth capabilities with the X-FEM. The phenomenon of spalling crack in thin-film structures is studied, and the application of the X-FEM to channel-cracking in thin films is conducted to show the relative ease with which strong singularities can be modeled within the partition of unity framework.

2.1. Center-crack in tension

As the first example, we model a center-cracked test specimen under pure tension. The model geometry shown in Fig. 1 consists of a plate of height $2h$ and width $2b$, with a center crack of length $2a$ ($\alpha = 90°$). For very large h and b ($h, b \gg a$), the mode I stress intensity factor K_I at the crack tip is $\sigma\sqrt{\pi a}$, where σ is the applied tensile stress on the remote boundary. For finite h and b, a dimensionless correction factor that depends on the ratio a/b is introduced for the SIF:

$$K_I = F(a/b)\sigma\sqrt{\pi a}. \tag{1}$$

The values of the correction factor for various ratios of a/b are listed in Tada et al. (2000). For example, if $a/b = 0.1$, then $F(a/b) = 1.006$. In addition, the value of the SIF is independent of the thickness of the specimen, so that both plane strain and plane stress approximations give the same SIF.

In Fig. 2, a structured and an unstructured mesh for the model geometry with $a/b = 0.1$ and $h/b = 1.5$ are illustrated. Due to symmetry, only half of the specimen is meshed. All enriched degrees of freedom associated with nodes on the essential boundary are set to zero. The structured mesh (Fig. 2a) consists of uniform bilinear quadrilateral elements (50×100 elements), whereas in the unstructured mesh (Fig. 2b

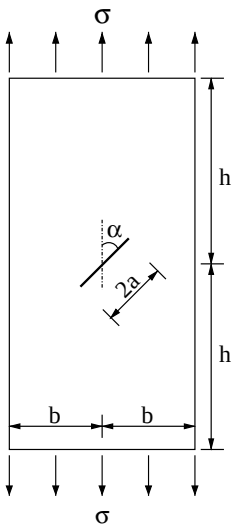

Fig. 1. Inclined crack under uniaxial tension.

and c), linear triangular finite elements (3362 elements with 1762 nodes) are used. The crack terminates on an element edge in the structured mesh (Fig. 2a), whereas in the unstructured mesh the crack-tip is in the interior of an element (Fig. 2c). In the rectangular mesh, the element size h_e is one-tenth of the crack length ($h_e = a/5$). The elastostatic boundary-value problem is solved using the X-FEM and the mode I SIF at the crack-tip is computed using the domain form of the interaction integral (see Part I for details). In Tables 1 and 2, the normalized SIF values are listed for different radii r_d of the integration domain used in the domain integral computations. In Table 1, we present results for the X-FEM with the Heaviside and near-tip enrichment functions, and also with only the Heaviside enrichment function. The use of the near-tip fields does lead to better accuracy; the comparison, however, would be more favorable for a crack in a finite domain in which a coarser mesh can be used. We observe that the K_I results are independent of the choice of the domain radius for radii r_d that are about twice or greater than the crack-tip element size. The numerical solution obtained on structured and unstructured meshes is in excellent agreement with the reference solution (Tada et al., 2000); the error is less than 1.0%.

2.2. Inclined crack in tension

As an example of a mixed mode crack problem, we consider an inclined crack ($2a = 2$) that is located at the center of a plate. The plate has dimensions 20×30 ($b = 10$, $h = 15$), and the crack is inclined at an angle α with respect to y-axis (Fig. 1). Uniaxial tension loading conditions are assumed ($\sigma_y = \sigma$). As a reference solution, we use the SIF solutions for an inclined crack in an infinite domain (Sih et al., 1962):

$$K_I = \sigma\sqrt{\pi a}\sin^2\alpha, \quad K_{II} = \sigma\sqrt{\pi a}\sin\alpha\cos\alpha. \tag{2}$$

In the numerical model, a uniform mesh consisting of 100×100 elements is considered. Numerical results for the SIFs are obtained for $\alpha = 15°, 30°, 45°, 60°, 75°$, and domain independence in the SIF computations is also studied. In Table 3, the normalized SIFs are compared to the reference solution (Sih et al., 1962). Excellent agreement between the numerical solution and the reference solution is obtained, and domain independence is realized for domain radii $r_d \geqslant 0.4$.

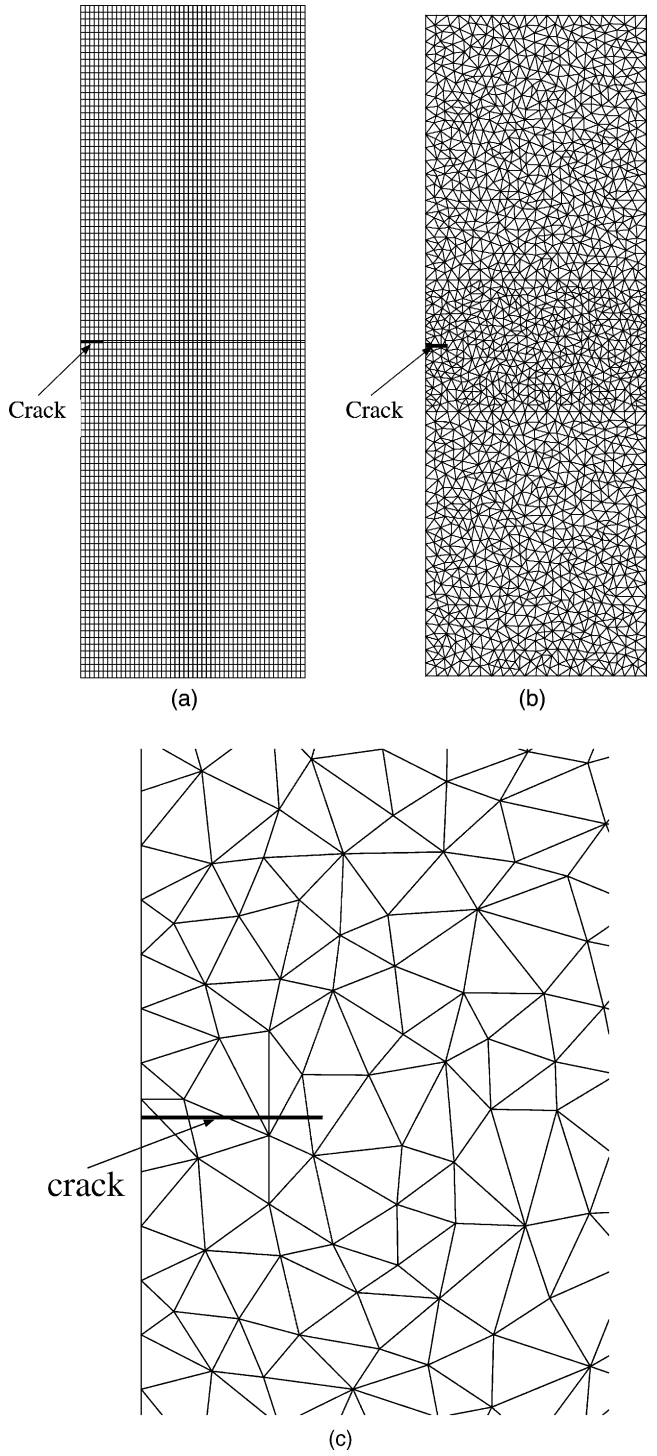

Fig. 2. Finite element meshes for the center-crack problem: (a) structured mesh; (b) unstructured mesh; and (c) unstructured mesh (vicinity of the crack).

Table 1
Normalized SIFs for the center-crack problem (structured mesh)

$\frac{r_d}{a}$	$\frac{K_I}{\sigma\sqrt{\pi a}}$ (X-FEM)	$\frac{K_I}{\sigma\sqrt{\pi a}}$ (X-FEM)$_H$
0.283	1.033	0.999
0.354	1.015	1.010
0.424	1.004	0.994
0.566	1.005	0.997
0.707	1.005	0.999

Table 2
Normalized SIFs for the center-crack problem (unstructured mesh)

$\frac{r_d}{a}$	$\frac{K_I}{\sigma\sqrt{\pi a}}$ (X-FEM)
0.424	1.023
0.573	1.000
0.716	0.992
0.859	0.994

Table 3
Normalized SIFs for the inclined crack problem

α	SIFs	Exact	X-FEM				
			$r_d = 0.2$	$r_d = 0.4$	$r_d = 0.6$	$r_d = 0.8$	$r_d = 1.0$
15°	$\frac{K_I}{\sigma\sqrt{\pi a}}$	0.0670	0.0565	0.0677	0.0681	0.0675	0.0673
	$\frac{K_{II}}{\sigma\sqrt{\pi a}}$	0.2500	0.2105	0.2656	0.2556	0.2458	0.2418
30°	$\frac{K_I}{\sigma\sqrt{\pi a}}$	0.2500	0.2651	0.2514	0.2518	0.2521	0.2516
	$\frac{K_{II}}{\sigma\sqrt{\pi a}}$	0.4330	0.4321	0.4331	0.4392	0.4384	0.4328
45°	$\frac{K_I}{\sigma\sqrt{\pi a}}$	0.5000	0.5007	0.4982	0.5025	0.5029	0.5029
	$\frac{K_{II}}{\sigma\sqrt{\pi a}}$	0.5000	0.5040	0.4978	0.4994	0.4997	0.5000
60°	$\frac{K_I}{\sigma\sqrt{\pi a}}$	0.7500	0.7711	0.7578	0.7535	0.7534	0.7538
	$\frac{K_{II}}{\sigma\sqrt{\pi a}}$	0.4330	0.4480	0.4307	0.4384	0.4372	0.4315
75°	$\frac{K_I}{\sigma\sqrt{\pi a}}$	0.9330	0.8724	0.9362	0.9356	0.9364	0.9367
	$\frac{K_{II}}{\sigma\sqrt{\pi a}}$	0.2500	0.1479	0.2595	0.2529	0.2444	0.2403

2.3. Arc-shaped cracks

Consider a circular crack AB of radius R and interior angle 2β in an infinite isotropic material under biaxial tension $\sigma_x^\infty = \sigma_y^\infty = \sigma$ at infinity (Fig. 3). The exact solution for the mixed mode SIFs is (Sih et al., 1962)

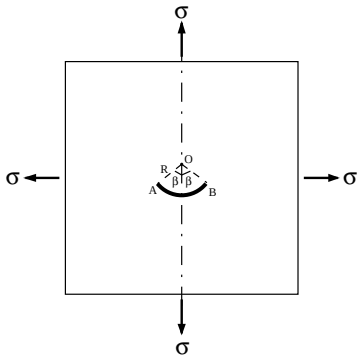

Fig. 3. Arc-shaped crack under far-field biaxial tension.

$$K_{\mathrm{I}} = \frac{\sigma}{1+\sin^2\frac{\beta}{2}}\left[\frac{\pi R\sin\beta(1+\cos\beta)}{2}\right]^{1/2}, \tag{3a}$$

$$K_{\mathrm{II}} = \frac{\sigma}{1+\sin^2\frac{\beta}{2}}\left[\frac{\pi R\sin\beta(1-\cos\beta)}{2}\right]^{1/2}. \tag{3b}$$

The sample geometry is 10×20 (half-model), and the arc radius $R = 1$. The finite element mesh consists of rectangular elements. In order to capture the curvature and to also model the infinite domain problem, a structured mesh with Cartesian grid refinement in a narrow band near the crack is used. In Fig. 4, the mesh in the vicinity of the crack is illustrated. The finite element mesh consists of 21,390 elements with a mesh size $h_{\mathrm{e}} = 0.02$ in the vicinity of the crack, and $h_{\mathrm{e}} = 0.26$ away from the crack. In the half-model, five linear segments are used to represent the crack for $\beta = 45°$, whereas for $\beta = 90°$, ten linear segments are adopted in the numerical simulations.

In Table 4, the mode I and mode II stress intensity factors are presented for different choices of the radii (r_{d}) in the domain integral computations. As opposed to the center-crack and inclined crack problems, a finer mesh is required for arc-shaped cracks due to the resolution of the crack curvature coupled with the

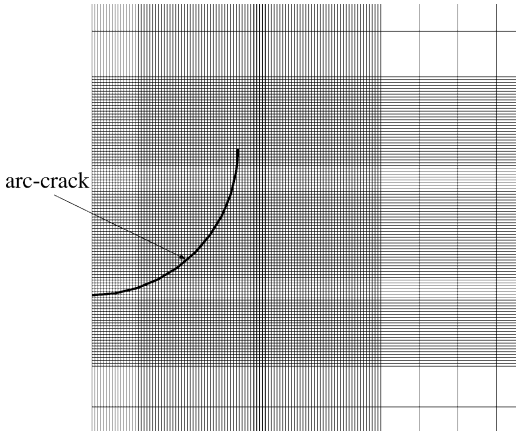

Fig. 4. Structured mesh in the vicinity of the crack for the arc-shaped crack problem ($\beta = 90°$).

Table 4
Normalized SIFs for the arc-shaped crack problem

β	SIFs	Exact	X-FEM		
			$r_d = 0.02$	$r_d = 0.04$	$r_d = 0.06$
45°	$\frac{K_I}{\sigma\sqrt{\pi R}}$	0.6776	0.6832	0.6965	0.6956
	$\frac{K_{II}}{\sigma\sqrt{\pi R}}$	0.2807	0.2869	0.2722	0.2717
90°	$\frac{K_I}{\sigma\sqrt{\pi R}}$	0.4714	0.5110	0.4982	0.4984
	$\frac{K_{II}}{\sigma\sqrt{\pi R}}$	0.4714	0.4582	0.4657	0.4653

fact that the crack size needs to be much smaller than the specimen dimensions to accurately represent the infinite domain problem. The X-FEM results are in good agreement with the reference solution. For domain sizes that vary up to the length of the crack-tip segment, domain independence is observed in the SIFs; the length of the crack-tip segment ($\beta = 90°$) is $\ell_c \approx 0.08$. Typically, when $r_d > \ell_c$, the presence of non-collinear crack segments (crack curvature) tends to deteriorate the accuracy in the SIFs. In the curved crack problem, there exists an interplay between the appropriate crack discretization, crack-tip element size, and the radius r_d used in the domain integral for the accurate evaluation of the SIFs. The above results are, however, not surprising since the J-integral is path-independent only for straight cracks; the use of appropriate path-independent integrals for curved (circular arc-shaped) cracks (Lorentzon and Eriksson, 2000) is required to attain domain independence in the SIF computations.

2.4. Double cantilever beam

In Fig. 5, a double cantilever beam is illustrated. By symmetry, a crack on the mid-plane of the sample is under pure mode I, and it would propagate straight ahead; however, this straight path is unstable. A crack lying slightly off the mid-plane tends to curve away from the mid-plane. In Fig. 5, the specimen dimensions are 6×2, and the initial pre-crack ($a = 2$) is placed slightly above the mid-plane of the cantilever beam. Quasi-static crack growth is governed by the maximum hoop stress criterion (Erdogan and Sih, 1963) (see Part I too), and the crack growth increment is $\Delta a = 0.1$. In Fig. 5, a representative crack growth simulation (120×41 mesh) for 11 steps is shown. In Belytschko and Black (1999) a similar simulation was considered,

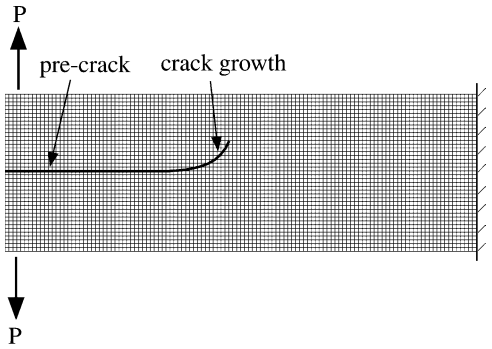

Fig. 5. Crack growth in double cantilever beam specimen.

with the crack-tip perturbed by an initial angle. The simulated crack path qualitatively agrees with experimental observations. The authors are unaware of any quantitative experimental results for comparison.

To study the influence of the mesh discretization, domain radius $r_d = r_k h_e$ (h_e is the crack-tip element size), and the crack growth increment Δa, a series of simulations were performed. The numerical results are illustrated in Fig. 6. In Fig. 6a, crack growth simulations for four different meshes are presented ($\Delta a = 0.1$ and $r_k = 1.5$); it is observed that under the given simulation conditions, the crack path is not mesh-sensitive. Domain independence is obtained in the numerical simulations with little difference as the domain radius is varied (Fig. 6b); the simulations are for the 360×121 mesh with $\Delta a = 0.1$. The influence of the crack growth increment Δa on the simulations is depicted in Fig. 6c. The results clearly indicate that Δa has the most pronounced effect on crack growth; for $\Delta a < 0.025$, the simulations are indistinguishable. On the basis of the above results, we can make the following inferences:

1. The mesh size, domain radius, and the crack increment should satisfy two conditions, namely (a) the domain radius should be at least 1.5 times the mesh size, and (b) the crack increment should be greater than the domain radius. These two conditions set an upper limit for the mesh size for a specific crack increment. Within this limit ($\Delta a > r_d > 1.5 h_e$), the results appear to be relatively insensitive to the mesh size.
2. The crack path depends on the crack increment, which is reasonable because we are modeling a smooth curve with a piece-wise linear approximation. Accuracy improves on using smaller Δa, but a smaller Δa requires a finer mesh. This is a consequence of the C^0 approximation for the crack and a limitation of the

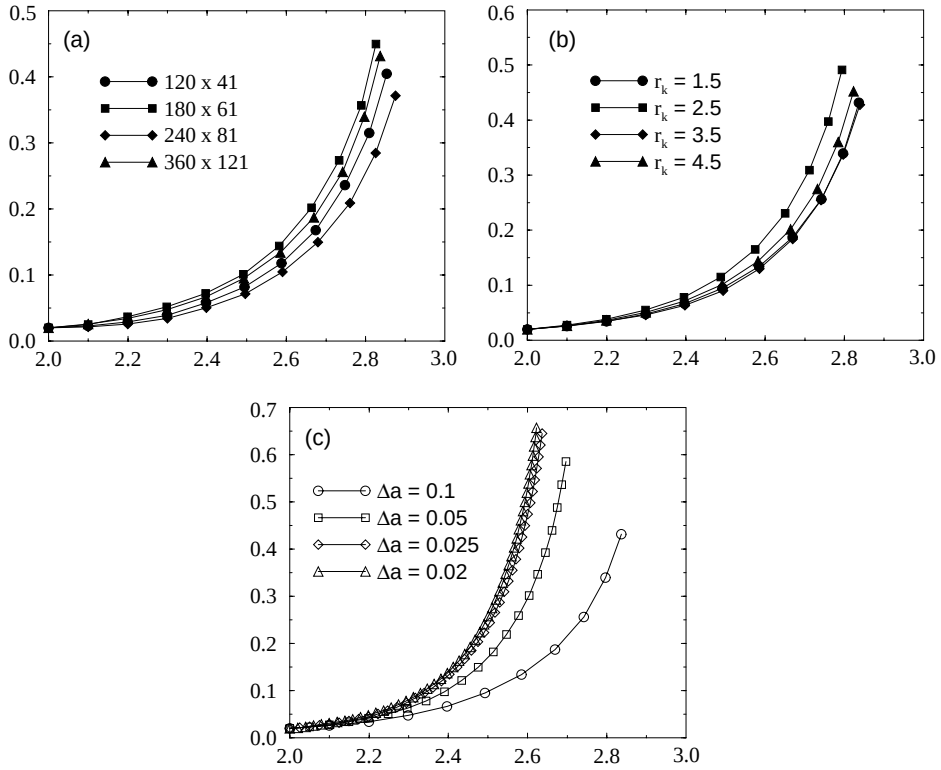

Fig. 6. Parametric study of simulated crack paths in double cantilever beam specimen: (a) influence of mesh discretization ($r_k = 1.5$, $\Delta a = 0.1$); (b) influence of domain radius (360×121 mesh, $\Delta a = 0.1$); and (c) influence of crack growth increment Δa (360×121 mesh, $r_k = 1.5$).

present implementation; the use of smooth representations of the crack and adoption of appropriate path-independent integrals for curved cracks are avenues that need to be explored for improvements in the crack growth capabilities with the X-FEM.

2.5. Mud-crack pattern

The simulation of multiple cracks in a brittle thin film bonded to an elastic substrate is carried out. A two-dimensional shear lag model is used to describe the deformation, which introduces the presence of a body force $\mathbf{b} = -\mu\mathbf{u}/hH$ in the model (Liang et al., 2003) (see Part I for the weak form). Here, $\mathbf{u}$ is the displacement vector, μ is the shear modulus of the substrate, and h and H are the thickness of the film and the substrate, respectively. The thin film is subjected to a biaxial initial stress ($\sigma^i_{11} = \sigma^i_{22} = \sigma$). In crack growth modeling of multiple cracks, a notion of time-dependence is required since the amount that each crack should grow is not known a priori. To meet this goal, a sub-critical crack growth law is used which is based on a V–G curve (velocity versus energy release rate). Crack growth is assumed to occur when the energy release rate $G > G_{\text{th}}$, and if $G < G_{\text{th}}$, the crack is stationary (G_{th} is a threshold value that is less than the critical energy release rate G_{c}). A path-independent contour integral (modified form of the J-integral) that includes the presence of the body force is proposed (Liang et al., 2003). Following Li et al. (1985), the contour integral is converted to its equivalent domain form to compute the energy release rate. For a given crack, the energy release rate at its tip is computed and on using the V–G relation, the velocity V^{c}_i at tip i is evaluated. The crack increment $\Delta a^{\text{c}}_i = V^{\text{c}}_i \Delta t$, where Δt is the time increment.

In the numerical model, we consider a domain $\Omega = (-5, 5)^2$ with a uniform mesh of 200×200 elements; the element size $h_{\text{e}} = 0.05$ (Fig. 7a). The spatial and temporal dimensions in the simulation are normalized with respect to the length and time scales in the model. The time step $\Delta t = 0.01$ and the simulations are carried out for 100 steps. We assume that the cracks do not intersect (cannot cross each other); if two cracks come closer than a distance $\epsilon = 10^{-4}$, then they cannot grow any further. In the domain integral

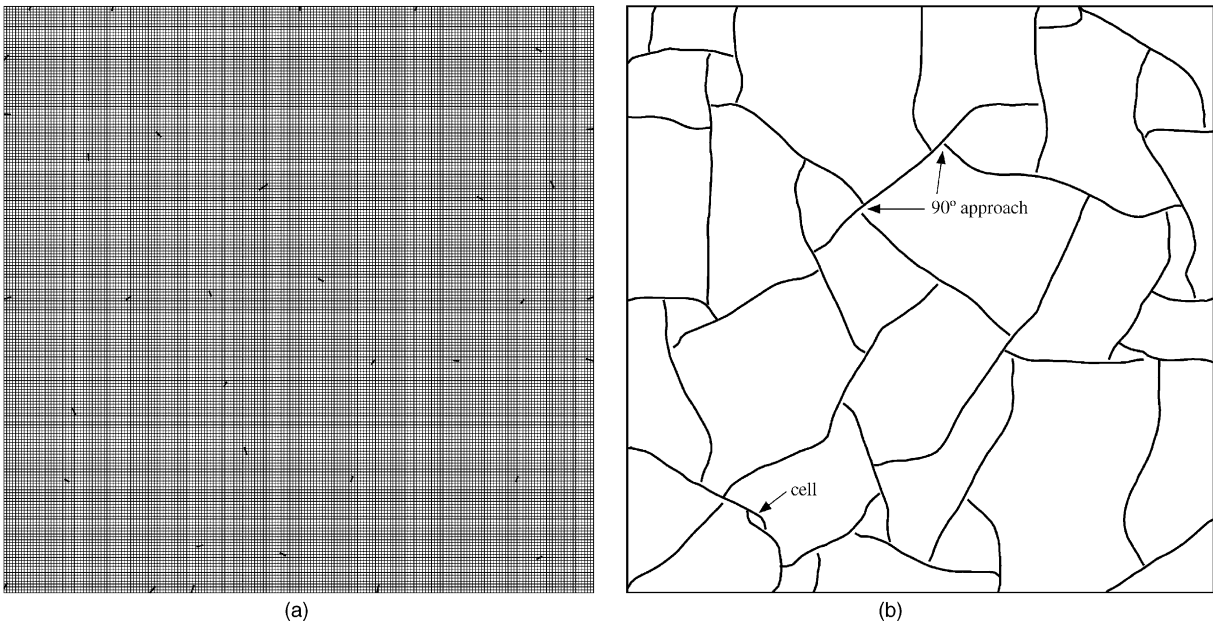

Fig. 7. Crack growth of multiple cracks (mud-crack pattern): (a) initial crack configuration; and (b) final configuration.

computations, $r_d = 0.075$ is chosen as the domain radius, and the maximum hoop stress criterion (Erdogan and Sih, 1963) is used to determine the crack growth direction. The initial crack configuration (35 cracks) is shown in Fig. 7a, and the final pattern is illustrated in Fig. 7b. In Liang et al. (2003), a different initial crack configuration and ensuing crack pattern is presented. From Fig. 7b, we observe that in most instances two cracks meet at right-angles, and when the crack-tips of two cracks are proximal, they tend to move towards each other and form small islands (cells) since the tip motion ceases.

2.6. Spalling of substrates

For a pre-tensioned thin film bonded to a thick brittle substrate, cracks originating from the edges have a tendency to divert into the substrate, and follow a trajectory parallel to the film-substrate interface. Such spalling cracks were observed experimentally by Cannon et al. (1986) in ceramic substrates and Thouless et al. (1987) in glass plates. Detailed experimental and analytical investigations of this problem have been conducted by Evans et al. (1990), Suo and Hutchinson (1989), and Chiao and Clarke (1990). For a film bonded to a semi-infinite substrate with the same elastic modulus, an analytical solution for the steady-state spalling was obtained by Hutchinson and Suo (1992), where the spalling depth is $d_{ss} = 2.86h$ (measured from the interface) and the mode I energy release rate is: $G_{ss} = 0.343\sigma^2 h/\overline{E}$. The film thickness is h, initial stress σ, Young's modulus E, Poisson's ratio v, and plane strain modulus $\overline{E} = E/(1-v^2)$. On considering the effect of elastic mismatch and finite substrate thickness, Suo and Hutchinson (1989) found that the spalling depth strongly depends on both the elastic mismatch and the substrate thickness but the dimensionless energy release rate is insensitive to the substrate thickness for $H/h > 10$.

The model problem with specimen dimensions is shown in Fig. 8a. The elastic modulus of the substrate and that of the film are the same, the substrate thickness is $H = 10h = 10$, and $L = 20$. An initial crack of length h is introduced at the edge below the interface. The reference solution for this problem is (Suo and Hutchinson, 1989)

$$G_{ss} = 0.281\sigma^2 h/\overline{E}, \quad d_{ss} = 1.05h. \tag{4}$$

For the model problem (Fig. 8a), $\sigma_{11}^i = \sigma$ is the only non-zero initial stress component in the thin film. In the X-FEM computations, a uniform mesh (200×110) is used. In Fig. 8b, the simulated (quasi-static crack growth conditions) crack path after 100 steps is illustrated. The crack path evolves and approaches the steady state. The depth of the steady-state crack is $d_{ss} = 1.026h$, and the computed energy release rate is

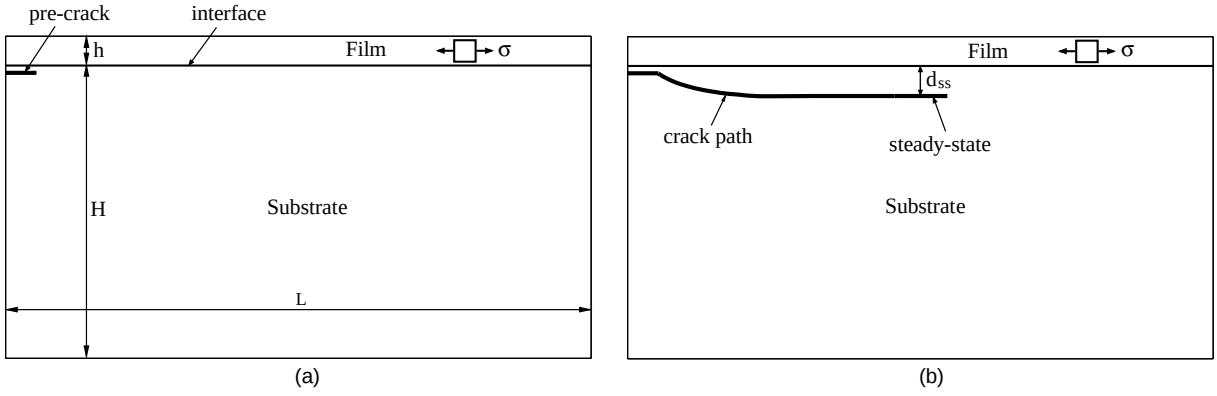

Fig. 8. Spalling of substrate: (a) initial crack and specimen dimensions; and (b) crack path until steady-state.

$G_{ss} = 0.284\sigma^2 h/\overline{E}$. The X-FEM results agree closely with the steady-state solution obtained by Suo and Hutchinson (1989), and the simulation also shows the transient stage of the crack growth.

2.7. Channel-cracking of thin films

Various crack patterns have been observed in thin-film structures, such as spalling of the substrate and channel-cracking of the film. In the case of channel-cracking, the crack channels through the film in the direction parallel to the interface, but arrests at the interface in the direction perpendicular to the interface, with the substrate being intact (Fig. 9). When the channel length exceeds a few times the film thickness, the crack reaches a steady-state, at which point the energy release rate can be computed from a 2-d plane strain problem, for example see Hutchinson and Suo (1992) and Huang et al. (2003). The steady-state energy release rate is given by (Hutchinson and Suo, 1992; Beuth, 1992)

$$G_{ss} = \frac{\sigma}{2h}\int_0^h \delta(y)\,\mathrm{d}y, \tag{5}$$

where $\delta(y)$ is the opening displacement. The plane strain problem involves a crack perpendicular to the interface with the tip at the interface. The stress singularity exponent for a crack terminating at a bimaterial interface depends on the elastic mismatch between the film and the substrate (Zak and Williams, 1963); the enrichment functions used in the X-FEM to model the crack-tip singularity for this problem was introduced in Huang et al. (2003), and a short description on the same appears in Part I.

The integral given in Eq. (5) is numerically evaluated to obtain the steady-state energy release rate. Results are presented in terms of the dimensionless driving force Z (Hutchinson and Suo, 1992; Evans et al., 1990):

$$G_{ss} = \frac{Z\sigma^2 h}{\overline{E}_1}, \tag{6}$$

where $\overline{E}_1$ is the plane strain modulus of the film. In Fig. 10, the dimensionless energy release rate Z is plotted as a function of the Dundurs parameter α; the Poisson's ratio of the thin film and the substrate are both equal to 1/3 and hence the other Dundurs parameter $\beta = \alpha/4$. The Dundurs parameters α are β are defined in Part I. The results in Fig. 10 are compared to a prior study by Beuth (1992) in which a dislocation-based formulation was adopted. The numerical results using X-FEM are in good agreement with the reference solution in Beuth (1992)—the difference is less than one percent for $\alpha < 0.9$ but higher for $\alpha > 0.9$. Compared to the approach pursued in Beuth (1992), the X-FEM allows one to analyze the effects of crack-spacing and finite substrate thickness.

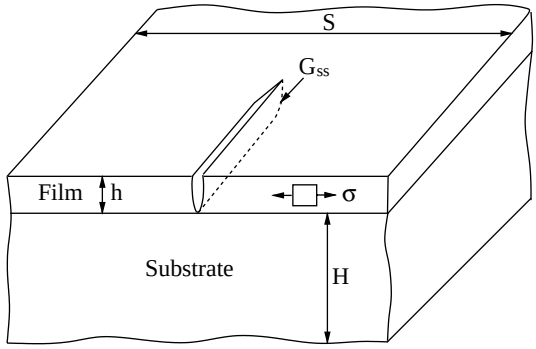

Fig. 9. Channel-cracking in a thin-film structure.

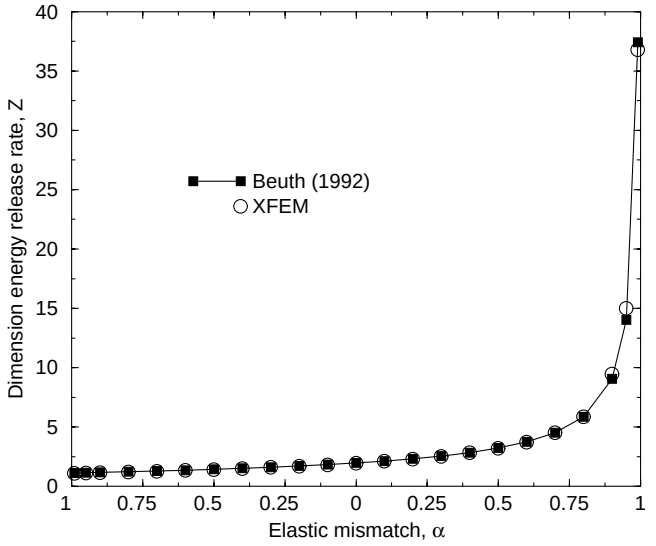

Fig. 10. Dimensionless energy release rate of a single channeling crack in a thin film bonded to a semi-infinite substrate.

To model channeling cracks in thin films bonded to compliant substrates using traditional finite elements is particularly challenging. When the substrate material is very compliant compared to the film, the stress singularity is much stronger ($\lambda > 1/2$) than the $\sqrt{r}$-singularity ($\lambda = 1/2$) for a crack in a homogeneous material ($\sigma_{ij} \sim r^{-\lambda}$). Typically, to resolve the strong stress singularity with finite elements an extremely fine mesh at the crack-tip is required, which in some instances might not be computationally feasible. To illustrate this, we compare the X-FEM computations with those obtained using the ABAQUS™ (Hibbit et al., 1993) finite element software. In the finite element calculations, eight-noded (bi-quadratic) quadrilateral elements are used with six-noded triangular elements in the vicinity (focused mesh) of the crack-tip. For the spacing $S/h = 4$ and $H/h = 2$, the dimensionless driving force Z is computed using the X-FEM and the FEM for $\alpha = 0$ (no mismatch) and $\alpha = 0.99$ (very compliant substrate). The results are listed in Table 5, where h is the film thickness and h_e is the mesh density (size) in the vicinity of the crack-tip. When $\alpha = 0$ and the crack-tip mesh density is about an order of magnitude greater than that used in the X-FEM, the difference in Z is less than one percent. However, when $\alpha = 0.99$ ($\lambda \sim 0.94$), the computations favor the X-FEM: in order to obtain about two percent difference in Z, the mesh density at the crack-tip in the finite element analysis is 10^6 times that used in the X-FEM. This disparity becomes significantly more pronounced with increasing values of the spacings S/h and H/h, as is the case for a single crack on a semi-infinite substrate (Huang et al., 2003).

Table 5
Comparison of energy release rate obtained using the FEM and the X-FEM for a channel-crack in a thin-film structure

Method	$\frac{h}{h_e}$	Z ($\alpha = 0$)	Z ($\alpha = 0.99$)
X-FEM	20	1.363	1.926
FEM	10^2	1.373	1.779
	10^3	1.374	1.819
	10^5	–	1.863
	10^7	–	1.882

The numerical examples we have presented in this paper are just a few of the many applications that are based on the X-FEM implementation described in Part I. The X-FEM has facilitated the modeling of new and challenging material failure problems in small structures (Huang et al., 2002, 2003; Liang et al., 2003, in press).

3. Conclusions

In Sukumar and Prévost (2003), we described a simple and robust means to model discontinuous fields (extended finite element method, X-FEM) within Dynaflow™, a finite element program. In the X-FEM (Moës et al., 1999), the crack is modeled through the displacement approximation using the framework of partition of unity (Melenk and Babuška, 1996). Crack modeling can be carried out without the need to mesh the crack surfaces, and in addition, no remeshing is required for crack growth problems. In this paper, we have presented numerical applications of the X-FEM to demonstrate the efficacy of our implementation and to show the capabilities of the method to solve challenging problems in computational failure mechanics.

Our focus in this paper was on computational fracture applications in isotropic and layered materials. Accurate stress intensity factor computations (mode I and mixed-mode) were obtained for benchmark problems such as the center-crack and the inclined crack under uniaxial tension. In addition, arc-shaped cracks under biaxial tension were also studied. Excellent domain independence in the SIF computations was realized for straight crack problems. For the arc-shaped cracks, appropriate choice of the crack representation, crack-tip element size, and the domain size used in the domain integral evaluation lead to accurate SIFs. The use of the path-independent form of the J-integral for circular arc-shaped cracks (Lorentzon and Eriksson, 2000) is required to obtain domain independence in the numerical (FEM or X-FEM) computations.

The crack growth capabilities of the X-FEM were demonstrated through growth simulations in the double cantilever beam specimen, complex mud-crack patterns that develop on an elastic substrate, and crack spalling in a thin-film structure. A parametric study of crack growth was performed in the double cantilever beam specimen. The numerical results revealed that the crack path was most sensitive to the crack increment, and for piece-wise linear approximations of the crack, the relation $\Delta a > r_{\mathrm{d}} > 1.5h_{\mathrm{e}}$ provided a reasonable guideline to obtain relatively mesh-insensitive crack growth results. In the layered material, the steady-state crack trajectory in the substrate was parallel to the thin-film interface which was in agreement with earlier findings. The crack driving force for a channel crack in a thin-film structure was also studied. The enrichment functions in the X-FEM were selected as those that span the asymptotic crack-tip displacement fields for a crack normal to and terminating at a bimaterial interface. The energy release rate of a single channeling crack in a thin film bonded to a semi-infinite substrate was obtained using the X-FEM, and the numerical results were found to be in good agreement with the reference solution (Beuth, 1992). A comparison of the X-FEM and the FEM for a channel crack impinging a compliant substrate was studied. The results revealed that for very compliant substrates ($0.9 < \alpha < 0.99$), the finite element method was not as competitive as the X-FEM and as $\alpha \to 0.99$, the FEM computations became prohibitively time-intensive.

Acknowledgements

The financial support to J.-H.P. and R.H. from the National Science Foundation through contract NSF-9988788, Dr. Jorn Larsen-Basse Program Manager, is gratefully acknowledged. Helpful discussions with Professor Zhigang Suo, and the assistance provided by Jim Liang and Dr. Zhenyu Huang with the

numerical computations are appreciated. The comments and suggestions of the anonymous reviewers are also acknowledged.

References

Belytschko, T., Black, T., 1999. Elastic crack growth in finite elements with minimal remeshing. International Journal for Numerical Methods in Engineering 45 (5), 601–620.

Beuth, J.L., 1992. Cracking of thin bonded films in residual tension. International Journal of Solids and Structures 29, 1657–1675.

Cannon, R.M., Fisher, R., Evans, A.G., 1986. Decohesion of thin films from ceramics. In: Materials Research Society Symposium Proceedings, vol. 54, pp. 799–804.

Chiao, Y.-H., Clarke, D.R., 1990. Residual stress induced fracture in glass–sapphire composites: planar geometry. Acta Metallurgica 38, 251–258.

Daux, C., Moës, N., Dolbow, J., Sukumar, N., Belytschko, T., 2000. Arbitrary cracks and holes with the extended finite element method. International Journal for Numerical Methods in Engineering 48 (12), 1741–1760.

Duarte, C.A., Oden, J.T., 1996. An *H–p* adaptive method using clouds. Computer Methods in Applied Mechanics and Engineering 139, 237–262.

Erdogan, F., Sih, G.C., 1963. On the crack extension in plates under plane loading and transverse shear. Journal of Basic Engineering 85, 519–527.

Evans, A.G., Drory, M.D., Hu, M.S., 1990. The cracking and decohesion of thin films. Journal of Materials Research 3 (5), 1043–1049.

Hibbit, D., Karlsson, B., Sorensen, P., 1993. ABAQUS User's Manual, Version 5.3. Paw-tucket, RI.

Huang, R., Prévost, J.H., Suo, Z., 2002. Loss of constraint on fracture in thin film structures due to creep. Acta Materialia 50, 4137–4148.

Huang, R., Prévost, J.H., Huang, Z.Y., Suo, Z., 2003. Channel-cracking of thin films with the extended finite element method. Engineering Fracture Mechanics 70 (18), 2513–2526.

Hutchinson, J.W., Suo, Z., 1992. Mixed mode cracking in layered materials. In: Hutchinson, J.W., Wu, T.Y. (Eds.), Advances in Applied Mechanics, vol. 29. Academic Press, Orlando, pp. 63–191.

Li, F.Z., Shih, C.F., Needleman, A., 1985. A comparison of methods for calculating energy release rates. Engineering Fracture Mechanics 21 (2), 405–421.

Liang, J., Huang, R., Prévost, J.H., Suo, Z., 2003. Evolving crack patterns in thin films with the extended finite element method. International Journal of Solids and Structures 40 (10), 2343–2354.

Liang, J., Huang, R., Prévost, J.H., Suo, Z., in press. Thin film cracking modulated by underlayer creep. Experimental Mechanics.

Lorentzon, M., Eriksson, K., 2000. A path independent integral for the crack extension force of the circular arc crack. International Journal of Fracture 66, 423–439.

Melenk, J.M., Babuška, I., 1996. The partition of unity finite element method: basic theory and applications. Computer Methods in Applied Mechanics and Engineering 139, 289–314.

Moës, N., Dolbow, J., Belytschko, T., 1999. A finite element method for crack growth without remeshing. International Journal for Numerical Methods in Engineering 46 (1), 131–150.

Prévost, J.-H., 1983. Dynaflow. Princeton University, Princeton, NJ 08544 (Updated Version: 2002).

Sih, G.C., Paris, P.C., Erdogan, F., 1962. Crack-tip stress intensity factors for plane extension and plane bending problems. Journal of Applied Mechanics 29, 306–312.

Sukumar, N., Prévost, J.-H., 2003. Modeling quasi-static crack growth with the extended finite element method. Part I: Computer implementation. International Journal of Solids and Structures, this issue.

Suo, Z., Hutchinson, J.W., 1989. Steady-state cracking in brittle substrates beneath adherent films. International Journal of Solids and Structures 25 (11), 1337–1353.

Tada, H., Paris, P.C., Irwin, G.R., 2000. The Stress Analysis of Cracks Handbook, third ed. ASME Press, New York.

Thouless, M.D., Evans, A.G., Ashby, M.F., Hutchinson, J.W., 1987. The edge cracking and spalling of brittle plates. Acta Metallurgica 35, 1331–1341.

Zak, A.R., Williams, M.L., 1963. Crack point singularities at a bimaterial interface. Journal of Applied Mechanics 30, 142–143.